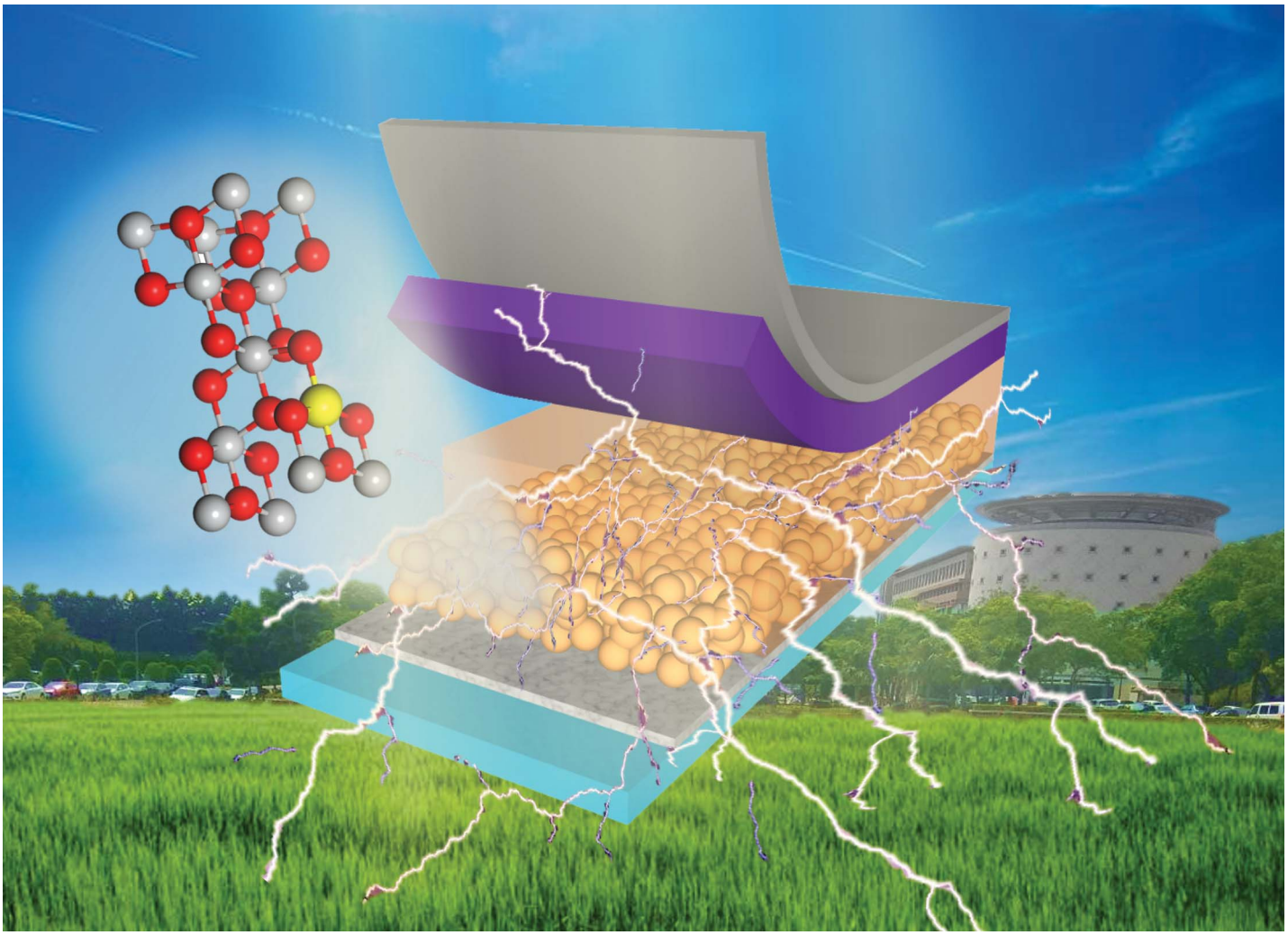

Showcasing research from Prof. Ming-Chung Wu and Prof. Kun-Mu Lee at Chang Gung University and Prof. Wei-Fang Su at National Taiwan University.

Enhancing the efficiency of perovskite solar cells using mesoscopic zinc-doped TiO_2 as the electron extraction layer through band alignment

The exceptional band alignment between perovskite active layer and meso-Zn:TiO_2 electron extraction layer can suppress the electron-hole recombination and improve electron transport behavior.

As featured in:

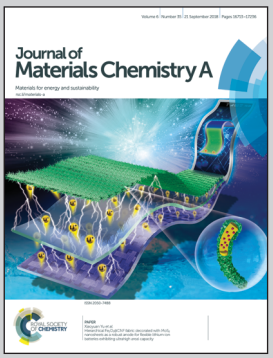

See Ming-Chung Wu, Kun-Mu Lee, Wei-Fang Su *et al.*, *J. Mater. Chem. A*, 2018, **6**, 16920.

ROYAL SOCIETY OF CHEMISTRY

rsc.li/materials-a

Registered charity number: 207890

Journal of Materials Chemistry A

PAPER

View Article Online
View Journal | View Issue

Cite this: J. Mater. Chem. A, 2018, 6, 16920

Enhancing the efficiency of perovskite solar cells using mesoscopic zinc-doped TiO_2 as the electron extraction layer through band alignment†

Ming-Chung Wu, ‡*abc Shun-Hsiang Chan,‡a Kun-Mu Lee, *abc Shih-Hsuan Chen,a Meng-Huan Jao,d Yang-Fang Chene and Wei-Fang Su *d

Received 5th June 2018
Accepted 24th July 2018

DOI: 10.1039/c8ta05291c

rsc.li/materials-a

Lead halide perovskite-structured solar cells (PSCs) have drawn great attention due to a rapid improvement in their photoelectric conversion efficiency in recent years. In this study, we have enhanced photovoltaic performance by using mesoscopic zinc-doped TiO_2 (meso-Zn:TiO_2) as the electron extraction layer. Zn:TiO_2 nanoparticles (Zn:TiO_2 NPs) with various zinc doping levels were synthesized by combining sol–gel and hydrothermal methods. The synthesized Zn:TiO_2 NPs were used to fabricate electron extraction layers by a screen-printing method. We systematically investigated the surface morphology, crystal structure, contact angle, charge carrier dynamics, electron mobility, and electrical conductivity of various meso-Zn:TiO_2. Furthermore, photo-assisted Kelvin probe force microscopy (KPFM) was used to analyze the surface potential of perovskite films coated with various meso-Zn:TiO_2 to understand the electron extraction behavior under the illumination of light at various wavelengths. Moreover, the energy levels of various meso-Zn:TiO_2 were estimated by ultraviolet photoelectron spectroscopy (UPS) and UV-vis absorption spectroscopy. We discovered that the 5.0 mol% meso-Zn:TiO_2 exhibited the optimal band alignment with perovskite. Finally, the average power conversion efficiency (PCE) of PSCs with meso-Zn:TiO_2 was enhanced from 13.1 to 16.8%, and such fabricated PSC yielded a champion PCE of 18.3%.

1. Introduction

Organic–inorganic hybrid perovskite-structured solar cells (PSCs) have generated tremendous interest in next-generation photovoltaics due to their high photoelectric conversion efficiency and solution processability.[1–3] Within a decade, the sparks of intensive research on PSCs have led to a dramatic increase of power conversion efficiency (PCE) to over 22%.[4,5] For an n-i-p structured PSC, the structure of the device is FTO/n-type material/absorber layer/p-type material/metal electrode. Among the various n-type materials, Al_2O_3,[6,7] ZnO,[8–10] ZrO_2,[11,12] SnO_2,[13–17] and TiO_2 (ref. 18–21) have been used as the electron extraction layer (EEL) because their appropriate energy bands align with the absorber layer. TiO_2 is the most commonly used EEL for next-generation photovoltaics because of its non-toxicity, chemical stability, inexpensiveness, and high charge transportability.[22–24]

The hysteresis of current density–voltage curves often occurs in planar n-i-p structured PSCs.[25] The hysteresis can lead to misjudgment of photovoltaic performance. Currently, the origin of *J–V* hysteresis of PSCs has been intensively studied. Such studies include charge accumulation at interfaces,[26,27] dielectric polarization by ferroelectric effects,[28] grain boundaries and capacitive effects,[29] and ion migration.[30,31] Various nanostructured materials, including nanorods,[32–34] nanotubes,[35,36] nanofibers,[37] nanowires,[38,39] and nanoparticles,[40–43] have been prepared to form the EEL, due to the easy formation of the mesoscopic structure and large surface area. The mesoscopic EEL exhibits a large contact area at the EEL/absorber layer (*i.e.*, $CH_3NH_3PbI_3$) interface for the reduction of charge accumulation and the balance of the electron and hole flux.[44,45]

Metal ion-doped TiO_2 can be used to enhance electrical conductivity and enhance the charge transport of PSCs. Various metal ion-doped TiO_2 materials, including niobium (Nb)-doped TiO_2,[46,47] yttrium (Y)-doped TiO_2,[48] magnesium (Mg)-doped TiO_2,[49] cobalt (Co)-doped TiO_2,[50] tin (Sn)-doped TiO_2,[51] tantalum (Ta)-doped TiO_2,[52] and lithium (Li)-doped TiO_2 (ref. 53), have

[a]Department of Chemical and Materials Engineering, Chang Gung University, Taoyuan 33302, Taiwan. E-mail: mingchungwu@mail.cgu.edu.tw; kmlee@mail.cgu.edu.tw; Fax: +886 3 2118800 ext. 5324; Tel: +886 3 2118800 ext. 3545; +886 3 2118800 ext. 3891

[b]Center for Reliability Sciences & Technologies, Chang Gung University, Taoyuan 33302, Taiwan

[c]Division of Neonatology, Department of Pediatrics, Chang Gung Memorial Hospital, Linkou, Taoyuan 33305, Taiwan

[d]Department of Materials Science and Engineering, National Taiwan University, Taipei 10617, Taiwan. E-mail: suwf@ntu.edu.tw; Fax: +886 2 23634562; Tel: +886 2 33664078

[e]Department of Physics, National Taiwan University, Taipei 10617, Taiwan

† Electronic supplementary information (ESI) available. See DOI: 10.1039/c8ta05291c

‡ M.-C. Wu and S.-H. Chan contributed equally.

been used to enhance the PCE of PSCs. Moreover, metal ion-doped TiO_2 can control the morphology, tune the optical bandgap,[54] and shift the conduction/valence band position.[55] Controlling the band alignment between the EEL and the absorber layer can effectively enhance the charge transport and reduce charge recombination.

Photo-assisted Kelvin probe force microscopy (KPFM) is an analysis technique to obtain the surface potential mapping of solar energy materials in the presence or the absence of illumination. For the photo-assisted KPFM measurements, a metal-coated probe scans the sample surface, and we can obtain the contact potential difference (CPD) between the sample and KPFM tip. However, there are only a few reports characterizing perovskite-structured materials using this unique technique.[56,57] The change of surface potential in the presence or the absence of illumination for solar energy materials is closely correlated to their photovoltaic performance. Thus, the photo-assisted KPFM technique provides a useful method to simply predict the photovoltaic performance of solar energy materials. The surface potential and electron injection ability of solar energy materials can be determined from the KPFM measurements. Therefore, the KPFM technique provides useful information for developing high-performance solar cells.

In our recent study, we fabricated highly conductive Zn-doped TiO_2 as a compact EEL of a PSC, achieving a PCE of 14.0%.[58] However, the planar n-i-p structured PSC with Zn-doped TiO_2 suffers from apparent *J–V* hysteresis. In the present work, we synthesized meso-Zn:TiO_2 as the EEL of a PSC by combining sol–gel and hydrothermal methods. Due to the hydrophilicity of meso-Zn:TiO_2, the perovskite-structured absorber layer coated on meso-Zn:TiO_2 presents higher crystallinity compared to non-doped meso-TiO_2. We also systematically studied the surface morphology, electron mobility, charge carrier dynamics, and electrical conductivity of various meso-Zn:TiO_2 EELs. To understand the electron extraction behavior between the perovskite-structured absorber layer and meso-Zn:TiO_2 EEL, the band levels and surface potentials of perovskite absorber layers are analyzed by UPS and photo-assisted KPFM, respectively. As a result, the average PCE of meso-Zn:TiO_2-based PSC was enhanced significantly, and such fabricated PSC yielded a champion PCE of 18.3%.

2. Experimental section

Synthesis of meso-Zn:TiO_2 pastes

12.5 g of titanium isopropoxide ($Ti(OCH(CH_3)_2)_4$, >97%, Sigma-Aldrich) was added to 5.0 mL of 2-propanol ($(CH_3)_2CHOH$, IPA, >99.8%, STAREK). 90.0 mL of 3.5 M acetic acid (CH_3COOH, >99.7%, Sigma-Aldrich) solution was prepared in another beaker. The acetic acid was then added to the titanium precursor solution, followed by continuous stirring in an ice bath for 12 h. The transparent solution was heated at 80 °C for 8 h, and the color of the solution became white translucent. This white translucent solution was treated in an autoclave at 170 °C for 6 h, and it was centrifuged to obtain TiO_2 NPs. 23.0 wt% TiO_2 NPs were mixed with α-terpineol ($C_{10}H_{18}O$, 90%, Merck) and ethyl cellulose (EC, ethoxyl content 48%, 22 cps, Acros). The excess solvent was then removed by rotary evaporation. For the synthesis of various Zn:TiO_2, zinc nitrate hexahydrate ($Zn(NO_3)_2 \cdot 6H_2O$, >97%, ECHO) was completely dissolved in 90.0 mL of the 3.5 M acetic acid solution at various stoichiometric ratios. Then, the above steps were repeated to obtain various meso-Zn:TiO_2 pastes.

Preparation of materials

All chemicals were used without further purification after purchasing from commercial sources. Methylammonium iodide (CH_3NH_3I, MAI) was synthesized according to a previous study.[59] $CH_3NH_3PbI_3$ was prepared by mixing MAI and lead iodide (PbI_2, 99.9985%, Alfa Aesar) at 1.70 M in a solvent mixture (50/50 v/v) of dimethyl sulfoxide (DMSO, 99.9%, ECHO) and γ-butyrolactone (GBL, ≥99%, Sigma-Aldrich) with continuous stirring at 35 °C for 12 h. 2,2′,7,7′-Tetrakis[*N*,*N*-di(4-methoxyphenyl)amino]-9,9′-spirobifluorene (spiro-OMeTAD, FrontMaterials) solution was prepared according to the literature.[60] For preparation of a dense TiO_2 precursor solution, 1.0 mL of titanium diisopropoxide bis(acetylacetonate) was added to 39.0 mL of ethanol (CH_3CH_2OH, >99.8%, Sigma-Aldrich).

Fabrication of the perovskite solar cells

FTO glass (7 Ω, Ruilong) was cleaned sequentially with detergent, methanol, 2-propanol, and UV-ozone treatment. The dense TiO_2 precursor solution was sprayed on the FTO glass at 450 °C. The dilute meso-Zn:TiO_2 paste (1/6 v/v in α-terpineol) was coated on dense TiO_2 by a doctor blade method and calcined at 500 °C for 30 min. The perovskite precursor solution was spin-coated onto the meso-Zn:TiO_2 at 1000 rpm for 10 s and at 5000 rpm for 20 s, respectively. After 17 s, 100 μL of toluene ($C_6H_5CH_3$, 99.8%, Sigma-Aldrich) was dropped on top of the perovskite absorber layer and annealed at 95 °C for 10 min. The spiro-OMeTAD solution was spin-coated over the perovskite absorber layer at 2500 rpm for 30 s. Finally, a silver electrode was thermally evaporated on the spiro-OMeTAD with a 0.09 cm^2 shadow mask.

Characterization of materials and devices

The *J–V* curves of the various PSCs were measured with a digital source meter (2400, Keithley) under simulated solar illumination at 100 mW cm^{-2}, AM 1.5G standard and with a calibrated Si-reference cell (Bunkokeiki, BS-520BK) with a KG-5 filter. The *J–V* curves were measured by reverse (from 1.2 to −0.2 V) and forward (from −0.2 to 1.2 V) scan. The step voltage was fixed at 10 mV and the delay time was fixed at 50 ms. The external quantum efficiency (EQE) spectra were recorded using an IPCE spectrometer (EQE-R-3011, Enli Technology Co. Ltd). The surface microstructure of various meso-Zn:TiO_2 was observed using a field-emission scanning electron microscope (FE-SEM) (JSM-7500F, JEOL) with an accelerating voltage of 10 kV. The surface potential mappings of various $CH_3NH_3PbI_3$/meso-Zn:TiO_2 were collected by KPFM (Dimension-3100 Multimode, Digital Instruments) with a Pt/Ir-coated tip in tapping mode. The KPFM measurements were performed under wavelength-switchable LED light source (WLS-LED, Mightex) illumination

at an angle of 45° (Fig. S1, ESI†). The absorption spectra were measured using a UV-vis spectrometer (V-730, Jasco). Synchrotron-based grazing-incidence wide-angle X-ray scattering (GIWAXS) patterns were collected by synchrotron X-ray spectroscopy ($\lambda \sim 1.0256$ Å) at beamline 13A1 of the National Synchrotron Radiation Research Center (NSRRC) in Hsinchu, Taiwan. The hydrophilicity of various meso-Zn:TiO_2 was evaluated using a water contact angle goniometer (100SB, Sindatek Instruments Co. Ltd). The steady-state photoluminescence (PL) spectra and time-resolved photoluminescence (TRPL) spectra were obtained by pumping the samples with a continuous-wave diode laser (λ_{exe} = 440 nm, PDLH-440-25, DONGWOO OPTRON). The transient TRPL plots were recorded using a time-correlated single photon counting (TCSPC) (WELLS-001 FX, DONGWOO OPTRON) spectrometer operated at a frequency of 312.5 MHz with 2 μs duration. Ultraviolet photoelectron spectroscopy (UPS, Sigma Probe, Thermo VG-Scientific) was used to analyze the valence band and the work function of various meso-Zn:TiO_2 with a UV source (HeI 0–21.2 eV).

3. Results and discussion

The surface microstructure and particle size distribution of various meso-Zn:TiO_2 coated on FTO glass are shown in Fig. 1a–e. Ethylene cellulose could be removed completely by thermal treatment at 500 °C. All of the meso-Zn:TiO_2 films exhibited a uniform porous structure. In addition, the particle size increased as the Zn doping level increased (Fig. 1f). When the Zn dopant concentration increased to 7.0 mol%, the particle size increased from 13.8 ± 2.7 nm (non-doped meso-TiO_2) to 17.5 ± 3.2 nm. The increase of particle size might be due to the different rates of hydrolysis and condensation when Zn was doped into TiO_2. The allowed insertions of Zn into the TiO_2 matrix must be determined by Pauling's rules. The $d_{(101)}$ spacing of anatase TiO_2 is also increased because the atomic radius of Zn^{2+} (74.0 pm) is larger than that of Ti^{4+} (60.5 pm).[61] The meso-Zn:TiO_2 architecture provided a porous support for the deposition and infiltration of the perovskite layer. Interestingly, many high-efficiency PSCs are essentially based on mesoporous device architectures.

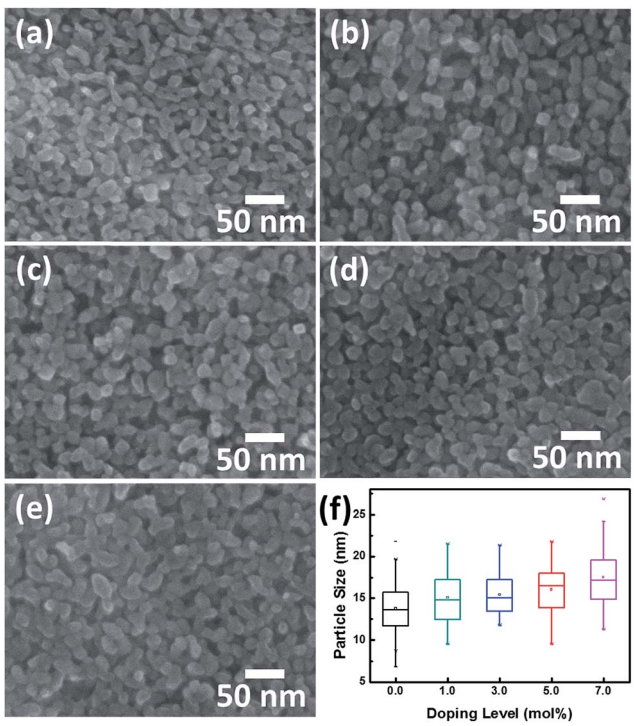

Fig. 1 The SEM images showing the surface microstructure of (a) non-doped meso-TiO_2 and various meso-Zn:TiO_2, including (b) 1.0 mol%, (c) 3.0 mol%, (d) 5.0 mol%, and (e) 7.0 mol%. (f) The particle size distribution of the meso-TiO_2 with various Zn doping levels.

The effect of Zn dopant on the crystal structure and crystallinity of meso-Zn:TiO_2 was measured. We found that all diffraction peaks of meso-Zn:TiO_2 can be indexed to the tetragonal anatase TiO_2 crystal structure (JCPDS Card no. 21-1272) (Fig. 2a). These results illustrated the incorporation of Zn ions into the anatase lattice. The signal of anatase TiO_2 (101) decreases when the Zn dopant concentration increases, indicating that the reduction in crystallinity is due to suppression of doped Zn in TiO_2 crystals.[62,63] In addition, the peak of anatase TiO_2 (101) slightly shifted to smaller scattering angles due to the larger ionic radius of Zn^{2+} (74.0 pm) compared with Ti^{4+} (60.5 pm). The UV-vis absorption spectra of various meso-Zn:TiO_2 are shown in Fig. 2b. There was a slight red shift of the absorption edge after Zn doping, which was consistent with the recent studies of T. T. Loan *et al.*, and D. V. Aware *et al.*, and our previous study.[58,62,64] The introduction of Zn can form a new band in the TiO_2 bandgap and change the electronic structure.[64] Hence, the bandgaps decreased from 3.74 eV (non-doped meso-TiO_2) to 3.67 eV (7.0 mol% meso-Zn:TiO_2) calculated from Tauc plots (Fig. 2c). The *J–V* curves of the PSCs with various meso-Zn:TiO_2 EELs are shown in Fig. 2d. The summary of photovoltaic characteristics is shown in Table 1. The open-circuit voltage (V_{oc}) increased from 0.98 to 1.06 V when the Zn doping level increased from 0.0 to 7.0 mol%. At the 5.0 mol% Zn-doping level, it led to the highest short-circuit current density (J_{sc}) of 21.6 mA cm^{-2}. Apparently, the photovoltaic performance was significantly enhanced by meso-Zn:TiO_2 with the optimal doping level. The average PCE of the PSC based on non-doped meso-TiO_2 is 13.0% (controlled device). When the Zn doping concentration increased to 5.0 mol%, the fill factor (FF) was significantly improved, and the average PCE was enhanced to 16.8%. We further confirmed the charge carrier dynamics of FTO/dense TiO_2/meso-Zn:TiO_2/$CH_3NH_3PbI_3$ by using the PL (Fig. 2e) and TRPL (Fig. 2f) spectra. The 5.0 mol% meso-Zn:TiO_2 sample showed the highest PL quenching. The decrease of PL intensity was attributed to efficient electron extraction from $CH_3NH_3PbI_3$ to TiO_2. We also measured the transient PL decay behavior of each sample. These results were adopted to investigate the charge transfer and separation behavior. The transient PL decay is fitted according to the exponential decay kinetics function:

$$F(t) = A\exp\left(-\frac{t}{\tau_1}\right) + B\exp\left(-\frac{t}{\tau_2}\right)$$

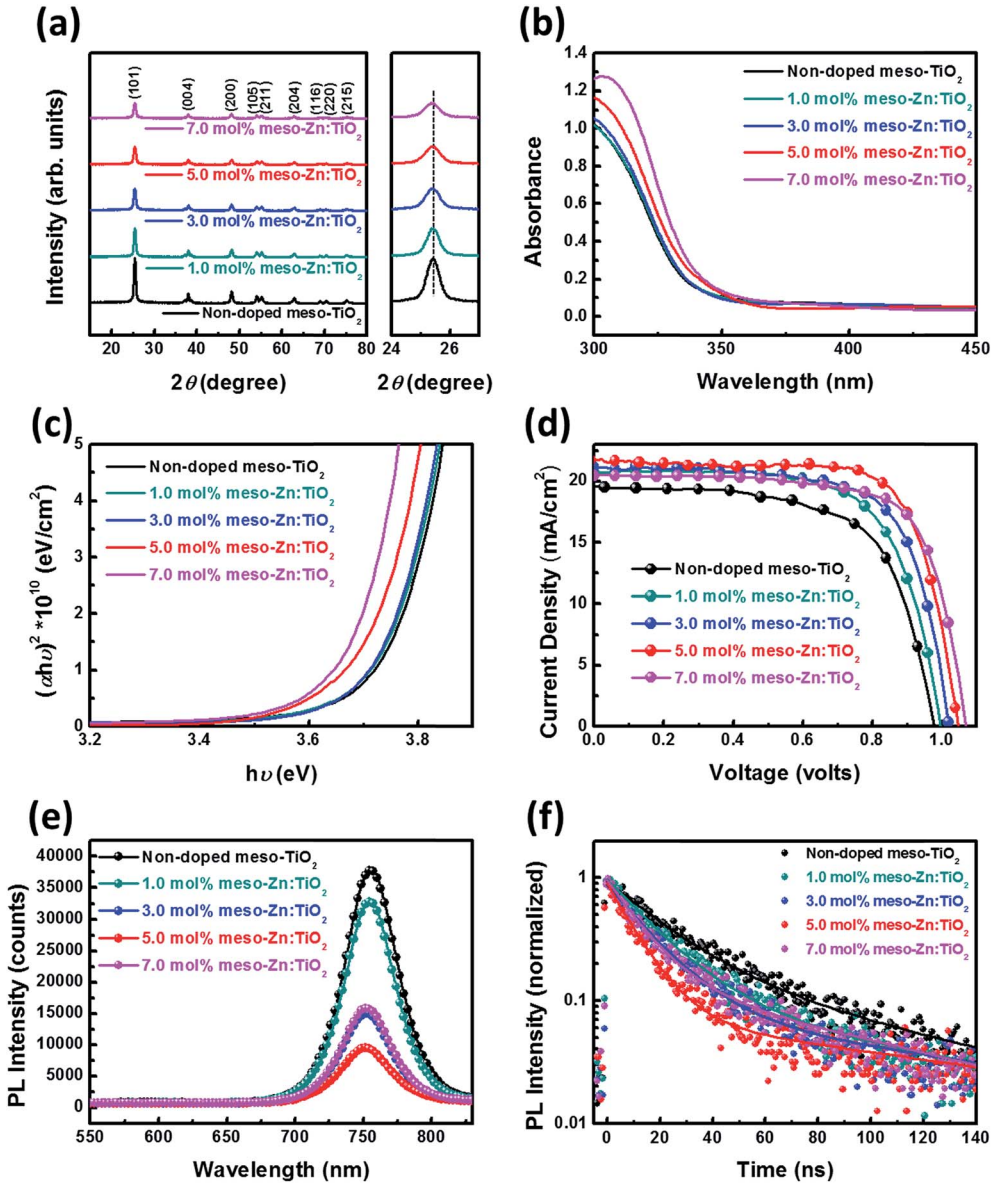

Fig. 2 (a) XRD patterns, (b) UV-vis absorption spectra, and (c) Tauc plots of various meso-Zn:TiO_2. (d) *J*–*V* curves of PSCs with various TiO_2-based EELs. (e) PL spectra and (f) transient TRPL plots of the $CH_3NH_3PbI_3$/meso-Zn:TiO_2/dense TiO_2/FTO structured device.

Table 1 Photovoltaic performance of various PSCs based on different EELs

Sample name	J_{sc} (mA cm^{-2})	V_{oc} (V)	FF (%)	PCE (%)
Non-doped meso-TiO_2	19.8 ± 0.6	0.98 ± 0.01	67.2 ± 2.4	13.0 ± 0.5
1.0 mol% meso-Zn:TiO_2	20.2 ± 0.4	1.00 ± 0.01	69.5 ± 1.5	14.0 ± 0.1
3.0 mol% meso-Zn:TiO_2	21.1 ± 0.2	1.03 ± 0.01	70.2 ± 1.2	15.2 ± 0.3
5.0 mol% meso-Zn:TiO_2	21.6 ± 0.6	1.05 ± 0.02	74.5 ± 1.6	16.8 ± 0.6
7.0 mol% meso-Zn:TiO_2	19.8 ± 0.5	1.06 ± 0.01	73.6 ± 2.0	15.4 ± 0.4

where *A* and *B* represent the time independent coefficient of the amplitude fraction, τ_1 is the fast decay time and τ_2 is the slow decay time.[65] The average PL lifetime (τ_{avg}) is calculated using the following equation:

$$\tau_{avg} = (A\tau_1 + B\tau_2)/(A + B)$$

The measured fast decay time, slow decay time, and PL average lifetime for $CH_3NH_3PbI_3$/meso-Zn:TiO_2/dense TiO_2/FTO are summarized in Table 2. The device with non-doped meso-TiO_2 showed a fast decay time of 18.7 ns, and the corresponding ratio was 64.1%. In contrast, the fast decay time of the device with 5.0 mol% meso-Zn:TiO_2 decreased to 8.8 ns, and the ratio

Table 2 Summary of the fast decay time (τ_1), slow decay time (τ_2), and PL average decay time (τ_{avg}) for $CH_3NH_3PbI_3$/meso-Zn:TiO_2/dense TiO_2/FTO

Sample name	A (%)	τ_1 (ns)	B (%)	τ_2 (ns)	τ_{avg} (ns)
Non-doped meso-TiO_2	64.1	18.7	35.9	92.0	45.1
1.0 mol% meso-Zn:TiO_2	72.8	14.1	27.2	51.8	24.3
3.0 mol% meso-Zn:TiO_2	80.8	13.5	19.2	67.2	23.8
5.0 mol% meso-Zn:TiO_2	83.8	8.8	16.2	61.2	17.3
7.0 mol% meso-Zn:TiO_2	80.1	11.5	19.9	69.1	23.0

increased to 83.8%. The 5.0 mol% meso-Zn:TiO_2 sample showed the shortest PL average lifetime of 17.3 ns. Thus, the 5.0 mol% meso-Zn:TiO_2 exhibited the highest charge separation rate and reduced radiative electron–hole recombination.

The valence and conduction band positions of various meso-Zn:TiO_2 were further analyzed by UPS (Fig. S2, ESI†). The energy level diagram of various meso-Zn:TiO_2 is shown in Fig. 3. The valence band maximum was estimated to have increased from −7.87 to −7.49 eV when the doping level was increased from 0.0 to 7.0 mol%, and the conduction band minimum shifted from −4.13 to −3.80 eV. However, the conduction band minimum of $CH_3NH_3PbI_3$ was found to be located at −3.90 eV. The electron injection from $CH_3NH_3PbI_3$ to 7.0 mol% meso-Zn:TiO_2 was hindered, so the electrons recombined in $CH_3NH_3PbI_3$ cause the increment of PL intensity (Fig. 2e) and average decay time (Fig. 2f). These results explained that the perovskite device with 7.0 mol% meso-Zn:TiO_2 showed lower J_{sc} and higher V_{oc}. Moreover, the conduction band minimum of 5.0 mol% meso-Zn:TiO_2 was close to that of $CH_3NH_3PbI_3$. The excellent band alignment between $CH_3NH_3PbI_3$ and 5.0 mol% meso-Zn:TiO_2 could improve the electron transfer efficiency.

We further investigated the orientation of the crystalline planes of $CH_3NH_3PbI_3$/meso-Zn:TiO_2 measured by synchrotron-based GIWAXS. The 2D GIWAXS pattern could fast collect the X-ray scattering data and crystal orientation. Fig. 4a and b display 2D GIWAXS patterns of the samples which consisted of $CH_3NH_3PbI_3$/meso-TiO_2/dense TiO_2/FTO with non-doped meso-TiO_2 and 5.0 mol% meso-Zn:TiO_2. The two kinds of samples exhibited the preferred orientation of perovskite crystallites with (110) and (220) showing intense signals in the q_z direction (Fig. S3, ESI†). Obviously, the $CH_3NH_3PbI_3$ layer with non-doped meso-TiO_2 displays a higher intensity of the undesired PbI_2 signal than the $CH_3NH_3PbI_3$ layer with 5.0 mol% meso-Zn:TiO_2. Fig. 4c shows the azimuthally integrated intensity plots of the 2D GIWAXS patterns in Fig. 4a and b. The $CH_3NH_3PbI_3$ layer with 5.0 mol% meso-Zn:TiO_2 demonstrated higher crystallinity of the tetragonal perovskite structure than that with non-doped meso-TiO_2. The static contact angles of water on meso-Zn:TiO_2 were measured to investigate the hydrophilic surface property between meso-Zn:TiO_2 and the $CH_3NH_3PbI_3$ layer (Fig. 4d and e). After Zn doping, the contact angle decreased from 31.2° to 20.6°, indicating that Zn doping could effectively improve the hydrophilicity of 5.0 mol% meso-Zn:TiO_2.[66] As the hydrophilic $CH_3NH_3PbI_3$ precursor solution was coated on the hydrophilic surface, the crystallinity of $CH_3NH_3PbI_3$ could be increased.[67]

We fabricated the samples of the $CH_3NH_3PbI_3$/meso-TiO_2/dense TiO_2/FTO structure with non-doped meso-TiO_2 and 5.0 mol% meso-Zn:TiO_2 for photo-assisted KPFM measurements. Fig. 5a and b show the topographic images of $CH_3NH_3PbI_3$ with non-doped meso-TiO_2 or 5.0 mol% meso-Zn:TiO_2. In order to better check the electron extraction capability, lights of various wavelengths were switched on and off during scanning. We measured the surface potential of $CH_3NH_3PbI_3$ deposited on various TiO_2 layers under each wavelength of light. The left column (Fig. 5c, e, g, i and k) shows the potential maps of $CH_3NH_3PbI_3$ with non-doped meso-TiO_2. In contrast, the right column (Fig. 5d, f, h, j and l) shows the surface potential mappings of $CH_3NH_3PbI_3$ with 5.0 mol% meso-Zn:TiO_2. When the $CH_3NH_3PbI_3$ absorbs photons carrying an energy higher than its bandgap, electrons and holes are generated. As the electrons transfer from $CH_3NH_3PbI_3$ to TiO_2, there will be a negative shift in the surface potential of $CH_3NH_3PbI_3$. Therefore, the change of surface potential can be used to evaluate the electron extraction ability. The work function of the tip and sample can be calculated using the following equation:[68]

$$\mathrm{CPD} = \frac{\phi_{\mathrm{tip}} - \phi_{\mathrm{sample}}}{e}$$

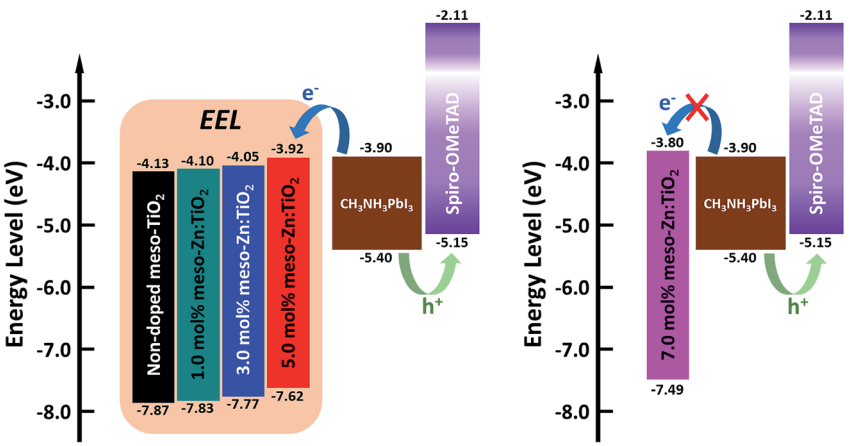

Fig. 3 Schematic energy level diagram of various meso-Zn:TiO_2 from UPS measurements (Fig. S2†).

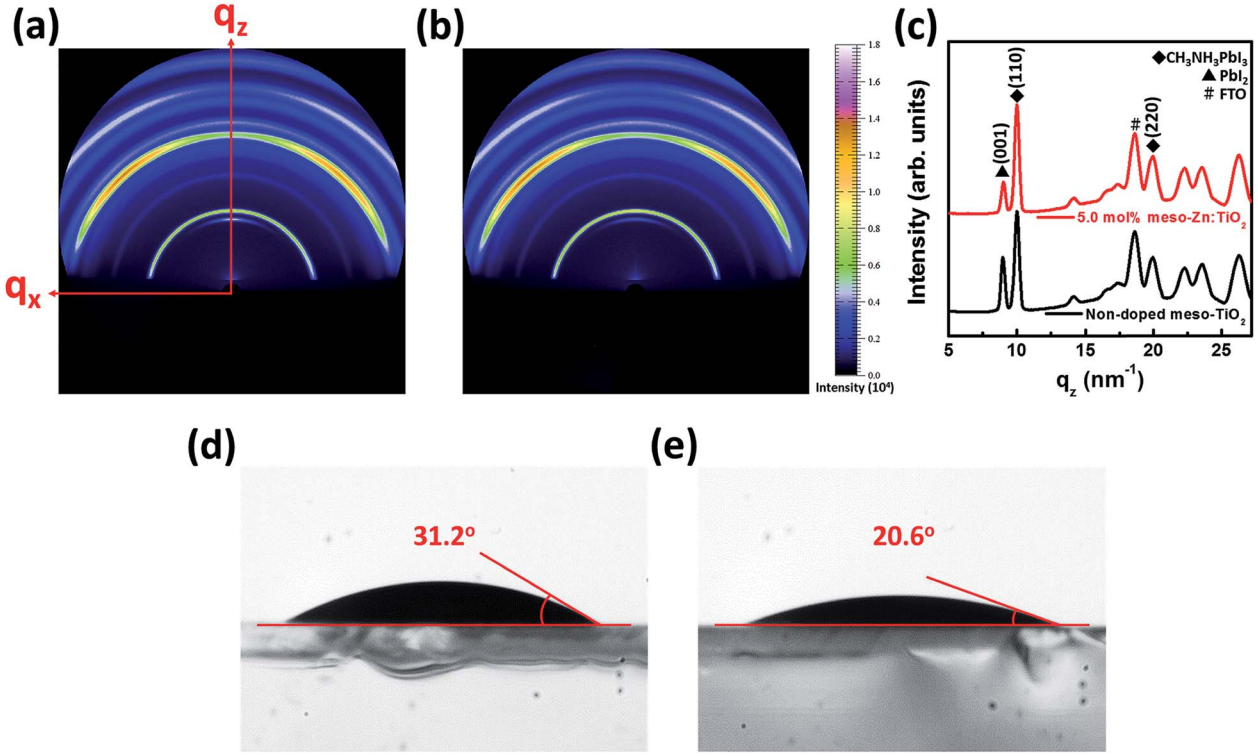

Fig. 4 2D GIWAXS patterns of $CH_3NH_3PbI_3$/meso-TiO_2/dense TiO_2/FTO with (a) non-doped meso-TiO_2 and (b) with 5.0 mol% meso-Zn:TiO_2. (c) 1D patterns of the out-of-plane line cut. The images of the contact angles of water on (d) non-doped meso-TiO_2 and (e) 5.0 mol% meso-Zn:TiO_2.

where ϕ_{tip} and ϕ_{sample} are the work function of the tip and sample, respectively, and e is the elementary charge (1.602×10^{-19} C). The work function of the Pt/Ir coated tip is ~5.0 eV by gold reference sample calibration. In Fig. 5c and d, the ΔCPD of $CH_3NH_3PbI_3$ with non-doped meso-TiO_2 (−42.1 mV) is less than that with 5.0 mol% meso-Zn:TiO_2 (−85.9 mV) under 470 nm light illumination. This result showed that more electrons were injected from $CH_3NH_3PbI_3$ to 5.0 mol% meso-Zn:TiO_2. Hence, the work function of $CH_3NH_3PbI_3$ with 5.0 mol% meso-Zn:TiO_2 increased more upon light illumination than that of $CH_3NH_3PbI_3$ with non-doped meso-TiO_2. Similarly, under 530 nm light illumination (Fig. 5e and f), the ΔCPD of the two samples decreased to −74.3 and −89.0 mV because $CH_3NH_3PbI_3$ exhibited a high conversion efficiency at this wavelength. When $CH_3NH_3PbI_3$ was subjected to 656 nm light irradiation, the ΔCPD slightly increased to −42.3 and −50.7 mV (Fig. 5g and h). We also used near-infrared light (850 nm) to irradiate $CH_3NH_3PbI_3$. There was no significant change (Fig. 5i and j) because the light energy at 850 nm is less than the bandgap of $CH_3NH_3PbI_3$. Finally, the CPD of $CH_3NH_3PbI_3$ with 5.0 mol% meso-Zn:TiO_2 revealed a significant shift (−126.2 mV) compared to that of non-doped meso-TiO_2 (−101.8 mV) under white light illumination. The ΔCPD of each sample is summarized in Fig. S4 (ESI†). The high CPD shift meant the effectiveness of electron transfer. Simultaneously, these results also meant that 5.0 mol% meso-Zn:TiO_2 demonstrated excellent electron extraction capability.

For the space-charge-limited current (SCLC) measurements, we fabricated electron-only devices that consisted of FTO/dense TiO_2/meso-TiO_2/Au with non-doped meso-TiO_2 and 5.0 mol% meso-Zn:TiO_2. An ~120 nm thick dense Au film was slowly deposited at a rate of 0.1 Å s^{-1}. The cross-sectional SEM image of the electron-only device is shown in Fig. S5 (ESI†). The I–V curves (Fig. 6a) are based on the analysis of three different regions: ohmic region ($I \propto V$), TFL region ($I \propto V^n$, $n > 2$), and Child's region ($I \propto V^2$). In the ohmic region (Fig. 6b), the I–V curves exhibit a linear behavior and follow $I = \sigma_0(A/d)V$, where A, d, and σ_0 are the sample area, thickness, and electrical conductivity, respectively. The electrical conductivity of the 5.0 mol% meso-Zn:TiO_2 sample (9.34×10^{-3} mS cm^{-1}) was found to be higher than that of the non-doped meso-TiO_2 sample (6.22×10^{-3} mS cm^{-1}). The transition point between the ohmic region and TFL region is named trap filled limit voltage (V_{TFL}). The relationship of V_{TFL} and trap density (N_t) is shown as follows:[69,70]

$$V_{TFL} = \frac{eN_t d^2}{2\varepsilon\varepsilon_0}$$

where e is the elementary charge, ε is the dielectric constant of TiO_2, and ε_0 is the permittivity of free space. The N_t of the non-doped meso-TiO_2 and 5.0 mol% meso-Zn:TiO_2 samples was found to be 3.88×10^{17} cm^{-3} and 3.02×10^{17} cm^{-3}, respectively. In the Child's region (Fig. 6c), the charge carrier mobility (μ) can be calculated using the Mott–Gurney law:[70,71]

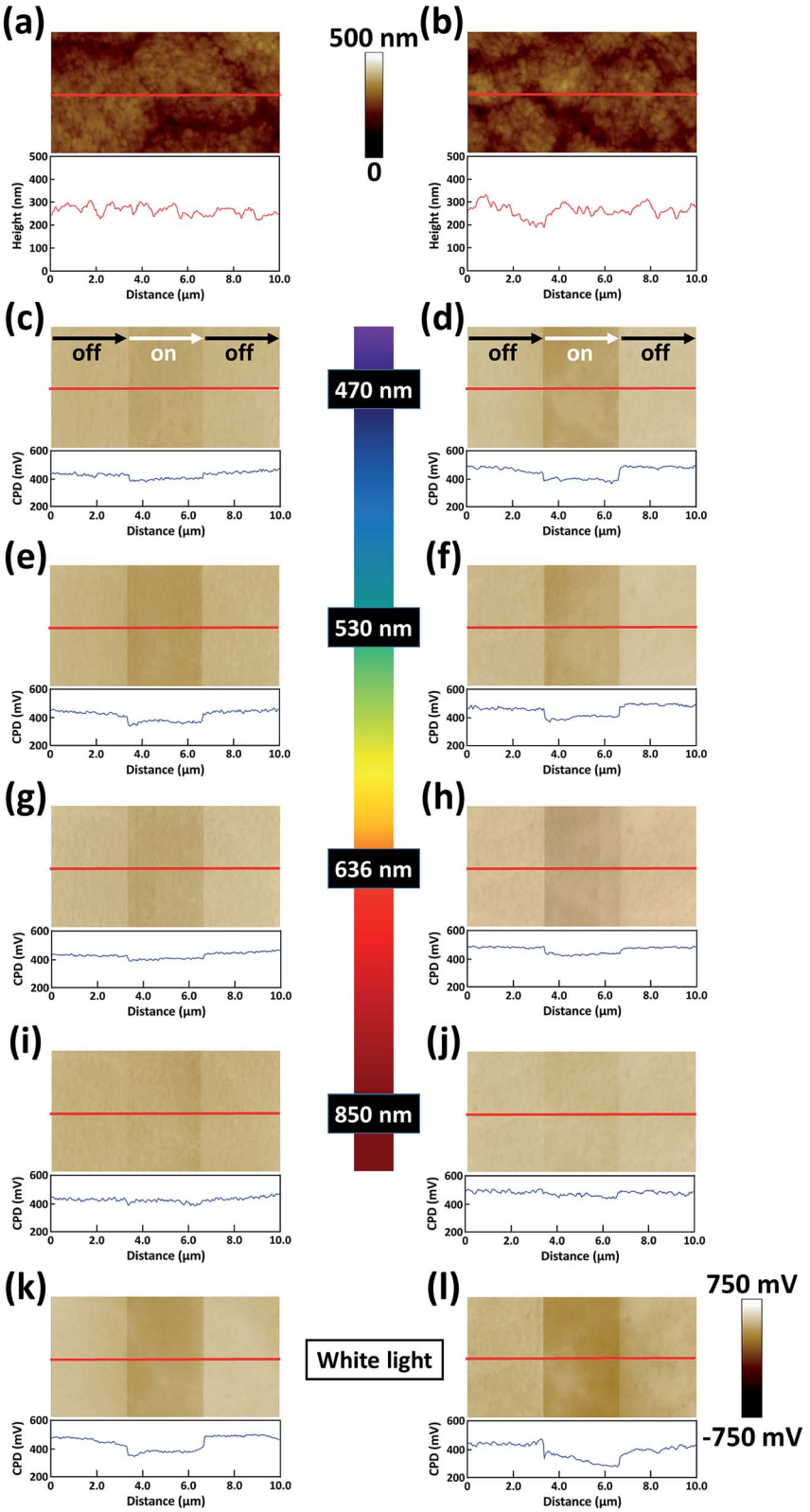

Fig. 5 AFM topographic image and cross-sectional measurements along the red line of two types of $CH_3NH_3PbI_3$/meso-TiO_2/dense TiO_2/FTO films with (a) non-doped meso-TiO_2 and (b) 5.0 mol% meso-Zn:TiO_2. The corresponding CPD images and cross-sectional analyses of CPD data under various wavelengths of light, including (c and d) 470 nm, (e and f) 530 nm, (g and h) 656 nm, (i and j) 850 nm, and (k and l) white light.

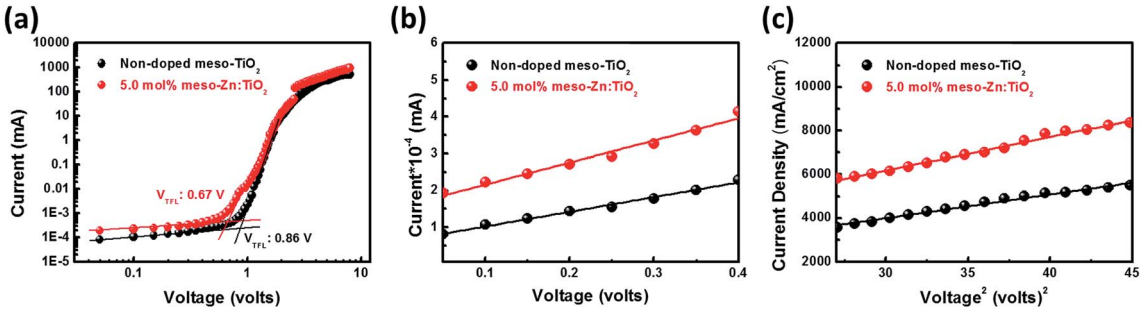

Fig. 6 (a) I–V curves of the device with the following structure: FTO/dense TiO_2/meso-TiO_2/Au with non-doped meso-TiO_2 and 5.0 mol% meso-Zn:TiO_2. (b) I–V curves of the ohmic region ($I \propto V$) and (c) J–V^2 curves of the Child's region ($I \propto V^2$).

$$J = \frac{9}{8}\mu\varepsilon\varepsilon_0\frac{V^2}{d^3}$$

The μ of the non-doped meso-TiO_2 and 5.0 mol% meso-Zn:TiO_2 samples was found to be 3.72×10^{-5} cm^2 V^{-1} s^{-1} and 5.27×10^{-5} cm^2 V^{-1} s^{-1}, respectively.

To understand the charge recombination mechanism of the perovskite devices with various meso-TiO_2 layers, light intensity-dependent J–V characteristics were investigated. Fig. 7a and b show V_{oc} and J_{sc} as a function of light intensity for the perovskite devices. J_{sc} shows a linear relationship with light intensity (Fig. 7a). The relationship between V_{oc} and light intensity is shown as follows:[72]

$$V_{oc} = V_s + \frac{nk_BT}{q}\ln\frac{P}{P_s}$$

where V_{oc} is the open-voltage at various light intensities, V_s is the open-voltage at 100 mW cm^{-2}, P represents various light intensities, P_s is the standard light intensity (100 mW cm^{-2}), n is the ideal factor, k_B is the Boltzmann constant, T is the absolute temperature (298.15 K), and q is the elementary charge. Fig. 7b demonstrates the semi-logarithmic plots of the V_{oc} *versus* incident light intensity, which shows the slopes of $1.42\frac{k_BT}{q}$ and $1.94\frac{k_BT}{q}$ for the two devices, respectively. The non-doped meso-TiO_2 EEL showed the slope of $1.94\frac{k_BT}{q}$, where n approached 2. In general, large n (~2) means that the trap assisted recombination is dominant in the perovskite device.[73,74] In contrast, the slope of $1.42\frac{k_BT}{q}$ for 5.0 mol% meso-Zn:TiO_2 suggested the reduction of trap assisted recombination.

The schematic diagram and cross-sectional SEM image of our perovskite device are shown in Fig. 8a and b, respectively. It has the configuration of FTO/dense TiO_2/meso-Zn:TiO_2/$CH_3NH_3PbI_3$/spiro-OMeTAD/Ag electrode. The thicknesses of meso-Zn:TiO_2, $CH_3NH_3PbI_3$, and spiro-OMeTAD are approximately 140, 320, and 190 nm, respectively. We also measured the J–V curves of PSCs under different scan direction (Fig. 8c). The perovskite device with 5.0 mol% meso-Zn:TiO_2 exhibited eliminated J–V hysteresis, because doping Zn ion into TiO_2 could effectively increase the conductivity and mobility, and reduce the trap density. We quantified the observed hysteresis to the hysteresis index (HI) for these two devices using the following equation:[75]

$$\mathrm{HI} = \frac{J_{RS}(0.8V_{oc}) - J_{FS}(0.8V_{oc})}{J_{RS}(0.8V_{oc})}$$

where $J_{RS}(0.8V_{oc})$ and $J_{FS}(0.8V_{oc})$ represent photocurrent density at 80% of V_{oc} for the reverse scan and forward scan, respectively. The PSC with 5.0 mol% meso-Zn:TiO_2 showed a smaller HI value of 0.083 compared to 0.397 for that of non-doped meso-TiO_2. To confirm the effect of meso-Zn:TiO_2 for better performance, we measured the PCE distribution of 16 devices with non-doped meso-TiO_2 and 16 devices with 5.0 mol% meso-

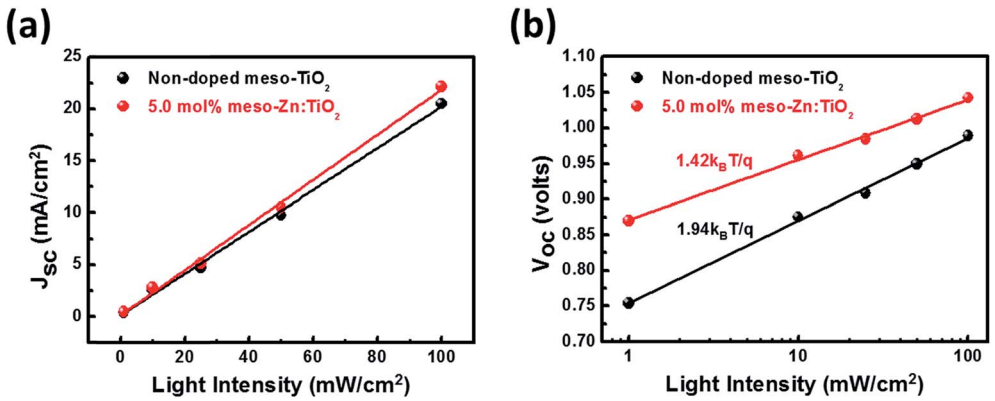

Fig. 7 Dependence of (a) J_{sc} and (b) V_{oc} on the light intensity of the PSCs with non-doped meso-TiO_2 and 5.0 mol% meso-Zn:TiO_2.

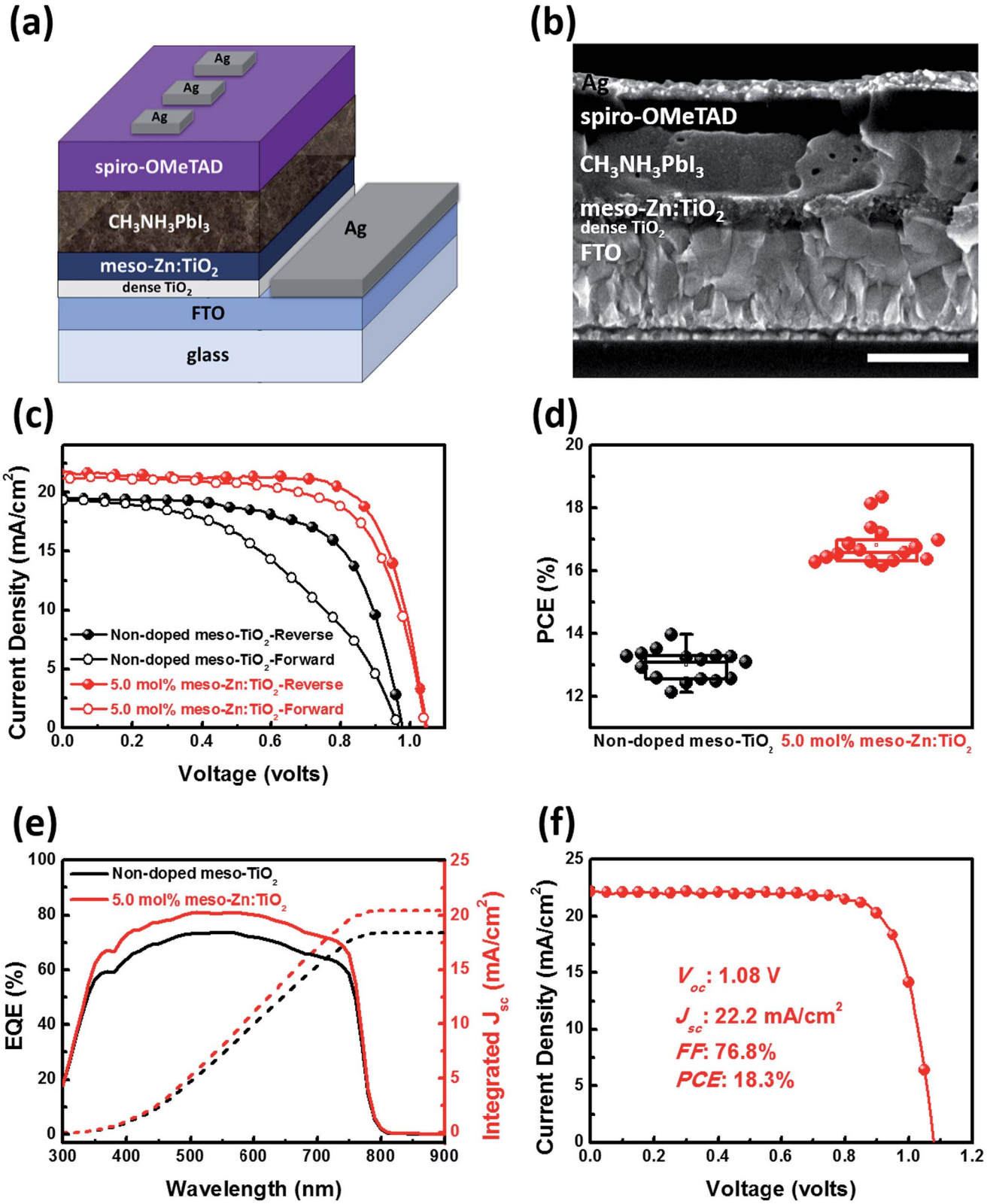

Fig. 8 (a) Schematic diagram and (b) cross-sectional SEM image of the PSC with 5.0 mol% meso-Zn:TiO_2 (scale bar = 500 nm). (c) *J*–*V* curves of the PSCs with non-doped meso-TiO_2 and 5.0 mol% meso-Zn:TiO_2 under reverse and forward scans. (d) PCE distribution and (e) EQE spectra of the PSCs with non-doped meso-TiO_2 and 5.0 mol% meso-Zn:TiO_2. (f) *J*–*V* curve of the champion device.

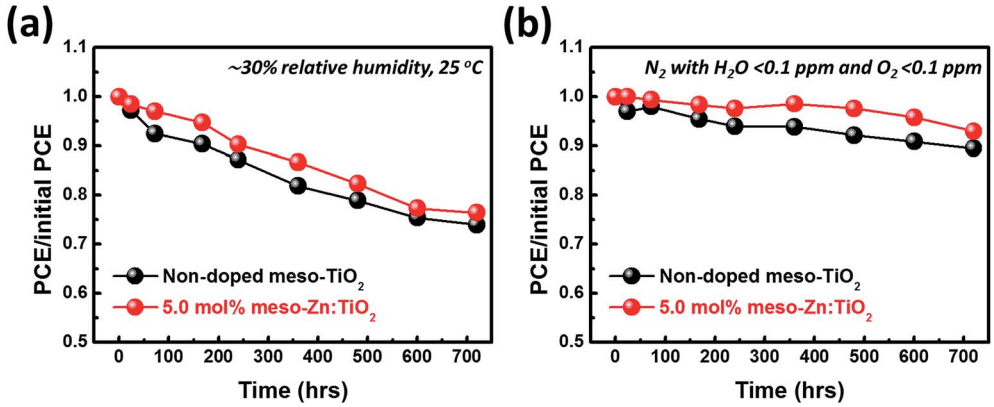

Fig. 9 Long-term stability of the PSCs with non-doped meso-TiO_2 and 5.0 mol% meso-Zn:TiO_2 (a) under the ambient atmosphere (~30% relative humidity, 25 °C) and (b) in the glovebox system (N_2 with H_2O < 0.1 ppm and O_2 < 0.1 ppm).

Zn:TiO_2 (Fig. 8d). From the EQE spectra shown in Fig. 8e, it can be confirmed that the improvement of electron injection from $CH_3NH_3PbI_3$ to 5.0 mol% meso-Zn:TiO_2 was caused by high conductivity and mobility. The integrated J_{sc} of the PSC with meso-Zn:TiO_2 (20.5 mA cm^{-2}) was found to be higher than that with meso-TiO_2 (18.4 mA cm^{-2}). The J_{sc} of the PSC measured using the EQE spectra is slightly lower than that measured using the *J–V* curves, because the UV region (<300 nm) of the EQE spectra is ignored. After optimizing the Zn doping concentration, the maximum efficiency was attained for a champion cell fabricated with 5.0 mol% meso-Zn:TiO_2, with $J_{sc} = 22.2$ mA cm^{-2}, $V_{oc} = 1.08$ V, FF = 76.8%, and PCE = 18.3% (Fig. 8f).

For the long-term stability test, the PSCs with non-doped meso-TiO_2 and 5.0 mol% meso-Zn:TiO_2 were stored in the ambient atmosphere (~30% relative humidity, 25 °C) and the glovebox system (N_2 with H_2O < 0.1 ppm and O_2 < 0.1 ppm). In the ambient atmosphere, the PSCs with non-doped meso-TiO_2 and 5.0 mol% meso-Zn:TiO_2 retained 74% and 76% of its initial PCE after 720 h, respectively (Fig. 9a). In the glovebox system (Fig. 9b), these PSCs exhibited high stability. Especially, the device with 5.0 mol% meso-Zn:TiO_2 still maintained ~92% of its initial PCE after 720 h due to the increment of $CH_3NH_3PbI_3$ crystallinity (Fig. 4).

4. Conclusion

We have successfully synthesized meso-Zn:TiO_2 NPs with various doping levels by combining sol–gel and hydrothermal methods, and they were used to fabricate EELs by a screen-printing method. The surface potential mapping of perovskite films with various meso-Zn:TiO_2 was performed by KPFM to predict the electron extraction behavior. The valence and conduction band positions of various meso-Zn:TiO_2 were further analyzed by UPS. The exceptional band alignment between the active layer and EEL could suppress the electron–hole recombination and improve the electron transfer behavior. After optimizing the processing conditions of the perovskite film coated with a 5.0 mol% meso-Zn:TiO_2 EEL, the average PCE was enhanced from 13.1 to 16.8%, and a PCE of 18.3% was achieved by the champion device with the 5.0 mol% meso-Zn:TiO_2 EEL.

Conflicts of interest

There are no conflicts of interest to declare.

Acknowledgements

The authors thank Dr Ming-Tao Lee's group (BL13A1) of the NSRRC at Taiwan for performing synchrotron-based X-ray diffraction and scattering techniques and grazing-incidence wide-angle X-ray scattering. The financial support from the Ministry of Science and Technology of Taiwan (Project No. 106-2221-E-182-057-MY3, 107-2119-M-002-012, and 106-2632-E-182-001) and Chang Gung Memorial Hospital, Linkou (CMRPD2H0171 and BMRPC74) is highly appreciated.

References

1 M. He, B. Li, X. Cui, B. Jiang, Y. He, Y. Chen, D. O'Neil, P. Szymanski, M. A. Ei-Sayed, J. Huang and Z. Lin, *Nat. Commun.*, 2017, **8**, 16045.
2 M. Ye, C. He, J. Iocozzia, X. Liu, X. Cui, X. Meng, M. Rager, X. Hong, X. Liu and Z. Lin, *J. Phys. D: Appl. Phys.*, 2017, **50**, 373002.
3 M. He, X. Pang, X. Liu, B. Jiang, Y. He, H. Snaith and Z. Lin, *Angew. Chem., Int. Ed.*, 2016, **55**, 4280–4284.
4 https://www.nrel.gov/pv/assets/images/efficiency-chart.png.
5 W. S. Yang, B.-W. Park, E. H. Jung, N. J. Jeon, Y. C. Kim, D. U. Lee, S. S. Shin, J. Seo, E. K. Kim, J. H. Noh and S. I. Seok, *Science*, 2017, **356**, 1376–1379.
6 M. M. Lee, J. Teuscher, T. Miyasaka, T. N. Murakami and H. J. Snaith, *Science*, 2012, **338**, 643–647.
7 Y. Wang, T. Mahmoudi, H.-Y. Yang, K. S. Bhat, J.-Y. Yoo and Y.-B. Hahn, *Nano Energy*, 2018, **49**, 59–66.
8 Q. An, P. Fassl, Y. J. Hofstetter, D. Becker-Koch, A. Bausch, P. E. Hopkinson and Y. Vaynzof, *Nano Energy*, 2017, **39**, 400–408.

9 P. Zhang, J. Wu, Y. Wang, H. Sarvari, D. Liu, Z. D. Chen and S. Li, *J. Mater. Chem. A*, 2017, **5**, 17368–17378.
10 Y.-Z. Zheng, E.-F. Zhao, F.-L. Meng, X.-S. Lai, X.-M. Dong, J.-J. Wu and X. Tao, *J. Mater. Chem. A*, 2017, **5**, 12416–12425.
11 M. A. Mejía Escobar, S. Pathak, J. Liu, H. J. Snaith and F. Jaramillo, *ACS Appl. Mater. Interfaces*, 2017, **9**, 2342–2349.
12 M. Che, L. Zhu, Y. L. Zhao, D. S. Yao, X. Q. Gu, J. Song and Y. H. Qiang, *Mater. Sci. Semicond. Process.*, 2016, **56**, 29–36.
13 K.-H. Jung, J.-Y. Seo, S. Lee, H. Shin and N.-G. Park, *J. Mater. Chem. A*, 2017, **5**, 24790–24803.
14 C. Xiao, C. Wang, W. Ke, B. P. Gorman, J. Ye, C.-S. Jiang, Y. Yan and M. M. Al-Jassim, *ACS Appl. Mater. Interfaces*, 2017, **9**, 38373–38380.
15 Q. Jiang, L. Zhang, H. Wang, X. Yang, J. Meng, H. Liu, Z. Yin, J. Wu, X. Zhang and J. You, *Nat. Energy*, 2016, **2**, 16177.
16 J.-W. Xiao, S. Ma, S. Yu, C. Zhou, P. Liu, Y. Chen, H. Zhou, Y. Li and Q. Chen, *Nano Energy*, 2018, **46**, 45–53.
17 H.-S. Rao, B.-X. Chen, W.-G. Li, Y.-F. Xu, H.-Y. Chen, D.-B. Kuang and C.-Y. Su, *Adv. Funct. Mater.*, 2015, **25**, 7200–7207.
18 Y. Yang, S. Feng, M. Li, F. Li, C. Zhang, Y. Han, L. Li, J. Yuan, L. Cao, Z. Wang, B. Sun and X. Gao, *Nano Energy*, 2018, **48**, 10–19.
19 J. R. Poindexter, R. L. Z. Hoye, L. Nienhaus, R. C. Kurchin, A. E. Morishige, E. E. Looney, A. Osherov, J.-P. Correa-Baena, B. Lai, V. Bulović, V. Stevanović, M. G. Bawendi and T. Buonassisi, *ACS Nano*, 2017, **11**, 7101–7109.
20 K. Wojciechowski, S. D. Stranks, A. Abate, G. Sadoughi, A. Sadhanala, N. Kopidakis, G. Rumbles, C.-Z. Li, R. H. Friend, A. K. Y. Jen and H. J. Snaith, *ACS Nano*, 2014, **8**, 12701–12709.
21 M. Singh, C.-H. Chiang, K. M. Boopathi, C. Hanmandlu, G. Li, C.-G. Wu, H.-C. Lin and C.-W. Chu, *J. Mater. Chem. A*, 2018, **6**, 7114–7122.
22 P. Docampo, S. Guldin, U. Steiner and H. J. Snaith, *J. Phys. Chem. Lett.*, 2013, **4**, 698–703.
23 M. He, D. Zheng, M. Wang, C. Lin and Z. Lin, *J. Mater. Chem. A*, 2014, **2**, 5994–6003.
24 X. Meng, C. Yu, X. Song, J. Iocozzia, J. Hong, M. Rager, H. Jin, S. Wang, L. Huang, J. Qiu and Z. Lin, *Angew. Chem., Int. Ed.*, 2018, **57**, 4682–4686.
25 N. K. Elumalai and A. Uddin, *Sol. Energy Mater. Sol. Cells*, 2016, **157**, 476–509.
26 B. Wu, K. Fu, N. Yantara, G. Xing, S. Sun, T. C. Sum and N. Mathews, *Adv. Energy Mater.*, 2015, **5**, 1500829.
27 K. Seki, *Appl. Phys. Lett.*, 2016, **109**, 033905.
28 A. M. A. Leguy, J. M. Frost, A. P. McMahon, V. G. Sakai, W. Kockelmann, C. Law, X. Li, F. Foglia, A. Walsh, B. C. O'Regan, J. Nelson, J. T. Cabral and P. R. F. Barnes, *Nat. Commun.*, 2015, **6**, 7124.
29 T. S. Sherkar, C. Momblona, L. Gil-Escrig, J. Ávila, M. Sessolo, H. J. Bolink and L. J. A. Koster, *ACS Energy Lett.*, 2017, **2**, 1214–1222.
30 T. Zhang, H. Chen, Y. Bai, S. Xiao, L. Zhu, C. Hu, Q. Xue and S. Yang, *Nano Energy*, 2016, **26**, 620–630.
31 P. Calado, A. M. Telford, D. Bryant, X. Li, J. Nelson, B. C. O'Regan and P. R. F. Barnes, *Nat. Commun.*, 2016, **7**, 13831.
32 X. Li, S.-M. Dai, P. Zhu, L.-L. Deng, S.-Y. Xie, Q. Cui, H. Chen, N. Wang and H. Lin, *ACS Appl. Mater. Interfaces*, 2016, **8**, 21358–21365.
33 T. Ujwal Kumar, M. A. Abdelrahman, K. Ryan, D. W. Benjamin, K. Piyush and S. Karthik, *Nanotechnology*, 2017, **28**, 274001.
34 A. Fakharuddin, F. Di Giacomo, A. L. Palma, F. Matteocci, I. Ahmed, S. Razza, A. D'Epifanio, S. Licoccia, J. Ismail, A. Di Carlo, T. M. Brown and R. Jose, *ACS Nano*, 2015, **9**, 8420–8429.
35 X. Wang, Z. Li, W. Xu, S. A. Kulkarni, S. K. Batabyal, S. Zhang, A. Cao and L. H. Wong, *Nano Energy*, 2015, **11**, 728–735.
36 T. T. Oo and S. Debnath, *AIP Conf. Proc.*, 2017, **1902**, 020015.
37 S. Dharani, H. K. Mulmudi, N. Yantara, P. T. Thu Trang, N. G. Park, M. Graetzel, S. Mhaisalkar, N. Mathews and P. P. Boix, *Nanoscale*, 2014, **6**, 1675–1679.
38 A. Dymshits, L. Iagher and L. Etgar, *Materials*, 2016, **9**, 60.
39 Y. Yu, J. Li, D. Geng, J. Wang, L. Zhang, T. L. Andrew, M. S. Arnold and X. Wang, *ACS Nano*, 2015, **9**, 564–572.
40 P. Chen, Y. Wang, M. Wang, X. Zhang, L. Wang and Y. Liu, *J. Energy Chem.*, 2015, **24**, 717–721.
41 J. Shao, S. Yang and Y. Liu, *ACS Appl. Mater. Interfaces*, 2017, **9**, 16202–16214.
42 T. Hwang, S. Lee, J. Kim, J. Kim, C. Kim, B. Shin and B. Park, *Nanoscale Res. Lett.*, 2017, **12**, 57.
43 J. Kim, T. Hwang, S. Lee, B. Lee, J. Kim, J. Kim, B. Gil and B. Park, *J. Appl. Phys.*, 2017, **122**, 145106.
44 D. Yang, X. Zhou, R. Yang, Z. Yang, W. Yu, X. Wang, C. Li, S. Liu and R. P. H. Chang, *Energy Environ. Sci.*, 2016, **9**, 3071–3078.
45 J. H. Heo, H. J. Han, D. Kim, T. K. Ahn and S. H. Im, *Energy Environ. Sci.*, 2015, **8**, 1602–1608.
46 M. Yang, R. Guo, K. Kadel, Y. Liu, K. O'Shea, R. Bone, X. Wang, J. He and W. Li, *J. Mater. Chem. A*, 2014, **2**, 19616–19622.
47 B.-X. Chen, H.-S. Rao, W.-G. Li, Y.-F. Xu, H.-Y. Chen, D.-B. Kuang and C.-Y. Su, *J. Mater. Chem. A*, 2016, **4**, 5647–5653.
48 P. Qin, A. L. Domanski, A. K. Chandiran, R. Berger, H.-J. Butt, M. I. Dar, T. Moehl, N. Tetreault, P. Gao, S. Ahmad, M. K. Nazeeruddin and M. Gratzel, *Nanoscale*, 2014, **6**, 1508–1514.
49 K. Manseki, T. Ikeya, A. Tamura, T. Ban, T. Sugiura and T. Yoshida, *RSC Adv.*, 2014, **4**, 9652–9655.
50 S. Sidhik, A. Cerdan Pasarán, D. Esparza, T. López Luke, R. Carriles and E. De la Rosa, *ACS Appl. Mater. Interfaces*, 2018, **10**, 3571–3580.
51 X. Zhang, Z. Bao, X. Tao, H. Sun, W. Chen and X. Zhou, *RSC Adv.*, 2014, **4**, 64001–64005.
52 Q. Cui, X. Zhao, H. Lin, L. Yang, H. Chen, Y. Zhang and X. Li, *Nanoscale*, 2017, **9**, 18897–18907.
53 F. Giordano, A. Abate, J. P. Correa Baena, M. Saliba, T. Matsui, S. H. Im, S. M. Zakeeruddin, M. K. Nazeeruddin, A. Hagfeldt and M. Graetzel, *Nat. Commun.*, 2016, **7**, 10379.

54 Y. Wang, R. Zhang, J. Li, L. Li and S. Lin, *Nanoscale Res. Lett.*, 2014, **9**, 46.
55 J. Wang, M. Qin, H. Tao, W. Ke, Z. Chen, J. Wan, P. Qin, L. Xiong, H. Lei, H. Yu and G. Fang, *Appl. Phys. Lett.*, 2015, **106**, 121104.
56 J.-J. Li, J.-Y. Ma, Q.-Q. Ge, J.-S. Hu, D. Wang and L.-J. Wan, *ACS Appl. Mater. Interfaces*, 2015, **7**, 28518–28523.
57 T. Hwang, B. Lee, J. Kim, S. Lee, B. Gil, A. J. Yun and B. Park, *Adv. Mater.*, 2018, **7**, 1704208.
58 M.-C. Wu, S.-H. Chan, M.-H. Jao and W.-F. Su, *Sol. Energy Mater. Sol. Cells*, 2016, **157**, 447–453.
59 S.-H. Chan, M.-C. Wu, K.-M. Lee, W.-C. Chen, T.-H. Lin and W.-F. Su, *J. Mater. Chem. A*, 2017, **5**, 18044–18052.
60 D. Liu and T. L. Kelly, *Nat. Photonics*, 2013, **8**, 133.
61 M. Salazar-Villanueva, A. Cruz-López, A. A. Zaldívar-Cadena, A. Tovar-Corona, M. L. Guevara-Romero and O. Vazquez-Cuchillo, *Mater. Sci. Semicond. Process.*, 2017, **58**, 8–14.
62 D. V. Aware and S. S. Jadhav, *Appl. Nanosci.*, 2016, **6**, 965–972.
63 K. Wu and J. Cui, *Optik*, 2018, **164**, 556–560.
64 T. T. Loan, V. H. Huong, V. T. Tham and N. N. Long, *Phys. B*, 2018, **532**, 210–215.
65 P. W. Liang, C. Y. Liao, C. C. Chueh, F. Zuo, S. T. Williams, X. K. Xin, J. Lin and A. K.-Y. Jen, *Adv. Mater.*, 2014, **26**, 3748–3754.
66 Z. Li, Y. Hou, B. Ma, X. Wu, Z. Xing and K. Li, *Environ. Prog. Sustainable Energy*, 2016, **35**, 1121–1124.
67 P. Li, C. Liang, Y. Zhang, F. Li, Y. Song and G. Shao, *ACS Appl. Mater. Interfaces*, 2016, **8**, 32574–32580.
68 W. Melitz, J. Shen, A. C. Kummel and S. Lee, *Surf. Sci. Rep.*, 2011, **66**, 1–27.
69 R. H. Bube, *J. Appl. Phys.*, 1962, **33**, 1733–1737.
70 J. H. Heo, M. S. You, M. H. Chang, W. Yin, T. K. Ahn, S.-J. Lee, S.-J. Sung, D. H. Kim and S. H. Im, *Nano Energy*, 2015, **15**, 530–539.
71 N. F. Mott and R. W. Gurney, *Electronic Processes in Ionic Crystals*, Oxford University Press, Oxford, 2nd edn, 1948.
72 F. Xie, C.-C. Chen, Y. Wu, X. Li, M. Cai, X. Liu, X. Yang and L. Han, *Energy Environ. Sci.*, 2017, **10**, 1942–1949.
73 J. Liu, G. Wang, Z. Song, X. He, K. Luo, Q. Ye, C. Liao and J. Mei, *J. Mater. Chem. A*, 2017, **5**, 9097–9106.
74 M. A. Contreras, K. Ramanathan, J. AbuShama, F. Hasoon, D. L. Young, B. Egaas and R. Noufi, *Prog. Photovoltaics*, 2005, **13**, 209–216.
75 H.-S. Kim and N.-G. Park, *J. Phys. Chem. Lett.*, 2014, **5**, 2927–2934.